

Modeling and Experimental Studies of Coating Delamination of Biodegradable Magnesium Alloy Cardiovascular Stents

Chenxin Chen,^{†,‡,§,Ⓧ} Jinyun Tan,^{†,⊥} Wei Wu,^{*,§,||} Lorenza Petrini,[#] Lei Zhang,[‡] Yongjuan Shi,[‡] Emanuele Cattarinuzzi,[§] Jia Pei,^{‡,Ⓧ} Hua Huang,^{‡,Ⓧ} Wenjiang Ding,[‡] Guangyin Yuan,^{*,‡,Ⓧ} and Francesco Migliavacca[§]

[‡]National Engineering Research Center of Light Alloy Net Forming & State Key Laboratory of Metal Matrix Composite, Shanghai Jiao Tong University, 800 Dongchuan Road, Shanghai, China, 200240

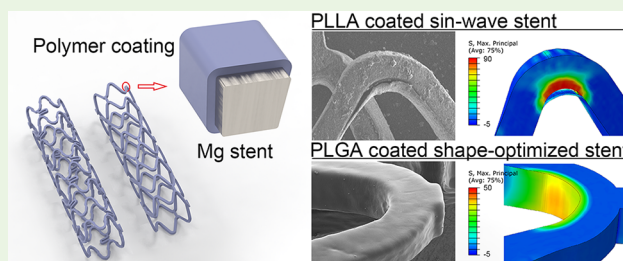
[§]Laboratory of Biological Structure Mechanics (Laboratories), Department of Chemistry, Materials and Chemical Engineering “Giulio Natta”, and [#]Department of Civil and Environmental Engineering, Politecnico di Milano, Piazza Leonardo da Vinci, 32, Milan 20133, Italy

[⊥]Department of Vascular Surgery, Huashan Hospital of Fudan University, No. 12 Mid-Wulumuqi Road, Shanghai 200040, China

^{||}Department of Mechanical Engineering, The University of Texas at San Antonio, One UTSA Circle, San Antonio, Texas 78249-0669, United States

ABSTRACT: Biodegradable magnesium alloy stents exhibit deficient corrosion period for clinic applications, making the protective polymer coating more crucial than drug-eluting stents with the permanent metal scaffold. We implemented a cohesive method based on a finite element analysis method to predict the integrity of adhesive between coating and stent during the crimping and deployment. For the first time, the three-dimensional quantitative modeling reveals the process of polymer coating delamination and stress concentration. The fracture and microcracks of coatings were consistent with the simulation result, confirmed by the scanning electron microscopy observation. Moreover, we analyzed four possible factors, i.e., stent design, strut material, coating polymer, and thickness of the coating, affecting the stent-coating damage and the distribution of the stress in coatings. Mg–Nd–Zn–Zr alloy with lower yield strength performed a more uniform strain distribution and more favorable adhesion of the coating than the commercial magnesium alloy AZ31. Shape optimization of stent design improves the strain and stress distribution of coating remarkably, avoiding coating delamination. Additionally, PLGA coating with lower elastic modulus and yield strength tends to follow the deformation of the stent better and to adhere on the surface more tightly, compared to PLLA polymer. A reduction in coating thickness and an increase in the strength of stent-coating interface improve the resistance to delamination. Our framework based on cohesive method provides an in-depth understanding of stent-coating damage and shows the way of computational analyses could be implemented in the design of coated biodegradable magnesium stents.

KEYWORDS: polymer coating, biodegradable magnesium alloy stent, delamination, cohesive zone method, finite element analysis



INTRODUCTION

In recent years, drug-eluting stents have become the standard therapy for percutaneous coronary intervention (PCI), to cure the treatment of coronary artery stenosis.^{1,2} Bioabsorbable polymer-based vascular scaffolds (BVS) and biodegradable magnesium alloy stents (BMS) were developed to overcome the shortcomings of drug-eluting stents, leaving no permanent implant with short-term support and long-term degradation to restore vessel function, avoiding a series of disadvantages.³ However, a series of clinical results of BVS show that the bioabsorbable polymer-based scaffold has noninferior rates of target lesion failure at 1 year to DES, but with a higher incidence of device thrombosis than the metallic stent through 2-year and 3-year clinical follow-ups.^{4–6} Considering the differentiating failure modes in metallic and polymeric devices,

BVS not only degrade but also possess significant localized structural irregularities that cause asymmetric degradation, which could be an explanation for the clinical results.⁷

Compared to the bioabsorbable aliphatic polymers of BVS, such as poly(L-lactic acid) (PLLA) and poly(D,L-lactic-co-glycolic acid) (PLGA), some of the biodegradable magnesium alloys have superior mechanical properties and uniform degradation process,^{8–11} which might lead to better long-term clinical behavior than that for BVS. However, the degradation rates of Mg alloys are still too high at the initial stage of implantation for the clinical requirements.^{12,13} On the

Received: June 18, 2018

Accepted: September 24, 2018

Published: September 24, 2018

one hand, applying polymer coatings on Mg alloys could reduce the degradation rate of Mg and carry antiproliferative drugs to avoid initial stenosis.^{14–17} In the light of observed coating damages on DES,^{18,19} the integrity and cohesion of polymer coating on BMS are more important, as the delamination or fracture of the coating would expose the Mg alloy strut surface and accelerate the localized corrosion rate, which might lead to vascular restenosis and prevent vessel endothelialization.^{19–21}

Finite element analysis (FEA) has been widely used to guide stent design and simulate the deformation and degradation of the implanted device.^{22–26} A cohesive zone method (CZM) based on a peeling model could efficiently reflect the adhesive property between two surfaces,^{27,28} for example, stent and coating. A series of 2D CZM simulation and experiments have been conducted for stainless drug-eluting stents to predict and explicate a variety of coating-damages, including delamination, webbing, and buckling.^{29–31} The CZM has also been applied to design and analyze coated biodegradable magnesium stent.^{26,32} Nevertheless, the previous simulations of the adhesion of polymer coatings and metallic stents are based on two-dimensional models. The specific deformation of coating in the thickness direction of stent and the effects of stent-balloon contact cannot be evaluated in such a model.

The present study aims to develop a 3D model to simulate the deformation process and stress distribution of polymer coatings, meanwhile predicting and evaluating the coatings integrity and delamination tendency. This work is carried out considering two Mg alloys: commercial Mg alloy AZ31 and Mg–Nd–Zn–Zr (abbr. JDBM), a magnesium alloy made by with excellent mechanical properties, and uniform degradation behavior.³³ High-quality microtubes,³⁴ stents,³⁵ and polymer coatings^{16,17} used in this work are progressed by the authors. The 3D FEA modeling for polymer-coated magnesium stent using CZM is first put forward to date.

MATERIALS AND METHODS

Stent Samples and Materials Properties. The chemical composition and processing of two magnesium alloy tubes, AZ31 and JDBM, can be found in our previous work.³⁴ Two designs, the stent with a sine-wave ring (abbr. SIN) and shape-optimized (abbr. OPT) stent designed by our group, are shown in Figure 1. The repeated units captured from each design to build the FEA mode are shown. The outer diameter and thickness of the stents were 3.00 mm and 160 μm , respectively.

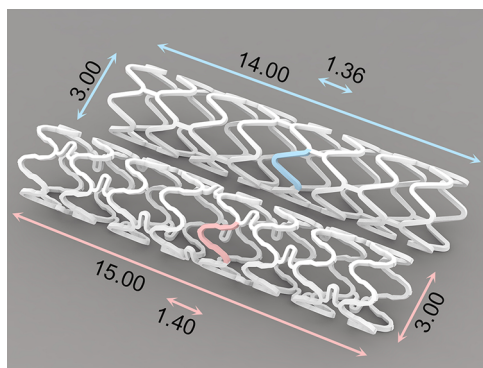


Figure 1. Geometries of SIN (top) and OPT stent (bottom) with the basic dimensions. One strut of each design (in red and blue highlight) was chosen for the modeling.

The AZ31 tubes were cut into SIN stents (abbr. AZ31-SIN), while the JDBM tubes were cut into OPT stents (abbr. JDBM-OPT). To adjust the unsmooth surface caused by the laser cutting, we polished the stents with the electrochemical method and then washed them via ultrasonic ethanol cleaning before drying.³⁴ After fluoride treatment of both AZ31-SIN and JDBM-OPT stents, the stents were prepared using an ultrasonic spray-coating technology as described in our previous work.¹⁷ Poly(L-lactic acid) (abbr. PLLA) and poly(lactic-co-glycolic acid) (abbr. PLGA) were used for stent coating spray. A total of 9 stents of three different groups, PLLA-coated AZ31-SIN, PLGA-coated AZ31-SIN, and PLGA-coated JDBM-OPT stents were crimped on the fold-balloon with an outer diameter of 1.3 mm. We inflated the balloon at the pressure of 8 atm to expand the coated stents with an outer diameter of 3.2 mm in the air. PLLA and PLGA with a weight-average molecular weight of $\sim 100\,000$ g/mol were bought from Jinan Daigang Biomaterial Co., Ltd. (Shandong, China). PLGA is in a mole ratio of LA/GA = 50/50. No drug is contained in those polymer coatings.

In our FEA model, JDBM and AZ31 alloy were used as stent platform materials, whereas PLLA and PLGA were used for the coating materials. The stress–strain curves of JDBM and AZ31 were obtained from tensile mechanical tests of microtubes.³⁴ The polymers' mechanical properties were taken from the study by Paryab et al.³⁶ The stress–strain curves are shown in Figure 2. The modulus of

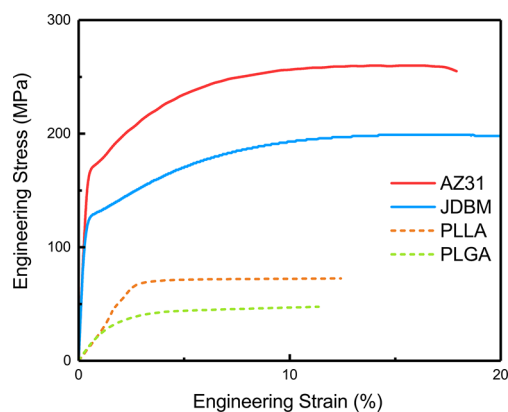


Figure 2. Stress–strain curves of AZ31 and JDBM stent materials, and PLLA and PLGA coatings.

elasticity and Poisson's ratio of magnesium alloys are 43.5 GPa and 0.35, respectively; the yield strength of JDBM and AZ31 are 120 and 175 MPa, respectively (Table 1).

Table 1. Materials Property in the FEA

parameters	stent		coating	
	AZ31	JDBM	PLLA	PLGA
density, ρ (kg m^{-3})	1.78	1.84	1.30	1.30
Young's modulus, E (GPa)	43.5	43.5	2.71	1.58
Poisson's ratio, ν	0.35	0.35	0.3	0.3
yield stress, σ (MPa)	175	122	67.9	29.7

Cohesive Zone Method (CZM). The CZM approximation describes the separation phenomenon caused by crack initiation and propagation between two surfaces. In this approach, the initial crack in the interface was valued by a traction-separation law, which is based on energy principles.²⁷ In FEA application, a single layer of cohesive elements (usually with a thickness of zero) is built between two surfaces as a “bonding” segment.³⁷ During the simulation, the cohesive elements resist the tensile loads, separating the adjoining surfaces until the initiation of damage and the potential failure of the elements.

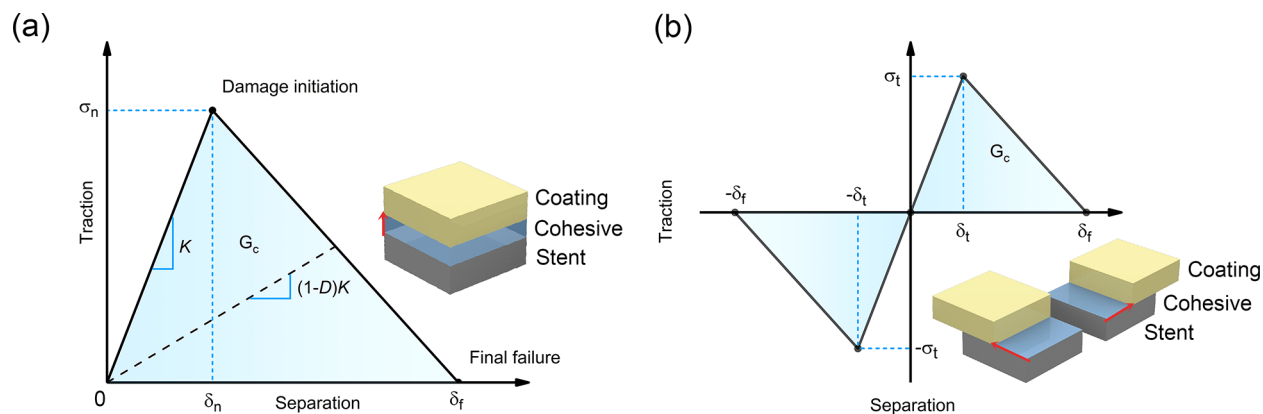


Figure 3. Schematic of the bilinear traction-separation law used for the cohesive elements, in the (a) normal and (b) tangential direction. Yellow and gray cubes stand for coating and stent elements, respectively. Red arrows show the traction direction.

A bilinear traction–separation law is applied in the CZM in this study. The pure model constitutive law of traction–separation responses in the normal direction and tangential direction is illustrated in Figure 3. This model assumes a linear elastic behavior before damage in the interface. Once an initiation criterion σ_n/σ_t is reached, the damage is initiated. Under continuous loading, damage spreads until the final fracture occurs.

The traction–separation constitutive relationship in normal separation can be expressed as

$$\sigma = \begin{cases} K\delta, & \delta \leq \delta_n \\ (1-D)K\delta, & \delta_n \leq \delta \leq \delta_f \\ 0, & \delta \geq \delta_f \end{cases} \quad (1)$$

and

$$D = \begin{cases} 0, & \delta \leq \delta_n \\ \frac{\delta - \delta_n}{\delta_f - \delta_n}, & \delta_n \leq \delta \leq \delta_f \\ 1, & \delta \geq \delta_f \end{cases} \quad (2)$$

where σ and δ are the stress and displacement of separation. δ_n and δ_f are the initial damage displacement and fracture displacement. D is a damage variable, overall scalar stiffness degradation, ranging from 0 to 1. K is the initial interfacial stiffness, which is treated as a penalty parameter and does not represent a physically measurable quantity.²⁸

The critical energy release rate G_c can be calculated by

$$G_c = \frac{1}{2}\sigma_n\delta_f \quad (3)$$

where σ_n is the interfacial critical stress.

In eqs 1–3, we assume that $\sigma_n = \sigma_v$ and $\delta_n = \delta_v$, so that the stresses, displacements, and critical fracture energy can be represented for the components in normal and tangential directions. In this simulation, the adhesion data is captured in an enhanced 90° peeling test, which is reported in our previous work by a penalty function method.^{28,38} The size of the peeling samples is 15 mm in length and 1 mm in width, whereas the critical release rate of the interface is 58.2 J/m². A peeling test with simultaneous imaging of the samples has been carried out by means of in-house-developed microtensile equipment.³⁹

Finite Element Model. Considering the symmetry of the stent, a one-sixth ring was developed for both SIN stent and OPT stent. Moreover, the influence of the balloon–stent interaction on coating delamination was investigated.

A theta-symmetry (Figure 4a) was applied to the nodes of the two distal surfaces of the structure and a radial displacement is applied to the balloon. The coating was modeled with a series thickness of 5, 10, and 15 μm covering the stents. Between the stent and the coating, and

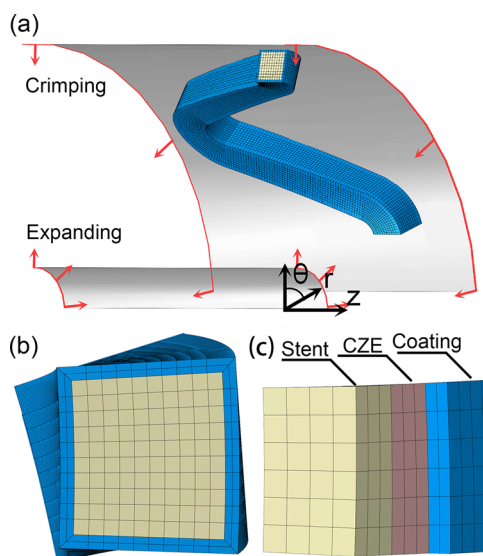


Figure 4. (a) FEA model of stent unit and two driving cylindrical surfaces, with boundary conditions in the circumferential direction and displacement loading in the radial direction. (b) Cross-section of the model includes stent (blue) and coating (yellow) meshes, and (c) cohesive zone element (red) between with zero thickness.

at the edge of coating, there is a monolayer of cohesive elements of zero thickness, as shown in Figure 4c. The balloon was modeled with a cylindrical surface. A general contact algorithm was applied to simulate interaction between coating and stent interaction, between abluminal side of coating and crimping device, and between luminal side of the coating and the balloon, setting a normal hard contact and a tangential behavior with a coefficient of friction of 0.2. In this way, the crimping and expansion deformation of the stent are driven by the inner and outer shells (Table 2).

The coating and stent were meshed with eight-node brick elements with reduced integration (C3D8R), 10 and 2 layers in the stent and coating thickness direction, respectively. The cohesive layer was meshed with eight-node tridimensional cohesive elements (COH3D8) with an average max edge length of 15 μm . And the balloon was meshed using four nodes surface elements with reduced integration (SFM3DR). The simulations were run using the ABAQUS/Explicit code 6.14 (Dassault Systèmes, Vélizy-Villacoublay, France).

SEM Characterization. The surface morphology of the PLLA and PLGA coatings were examined by scanning electron microscopy (SEM, JSM 7600F, Japan). Before SEM observation, samples were coated with a layer of gold with a thickness of ~ 20 nm by a sputter coater (SHINKKU VD MSP-1S, Japan).

Table 2. Boundary Conditions for Stent-Coating Deformation

time (s)	outer surface (crimping)		inner surface (expansion)	
	diameter (mm)	contact state	diameter (mm)	contact state
0	3.1	✓		
0.5	3.0	✓		
1.5	1.3	✓	1.1	✓
2.0			1.1	✓
3.5			3.1	✓
4.0				

Objectives of the Study. First, three FEA scenarios were simulated and validated by experiments: the AZ31-SIN stent coated with PLLA and PLGA, respectively, and the JDBM-OPT stent coated with PLGA. Only two stent platforms were provided because of the difficulty in manufacturing stent samples. The thickness of the coatings is 10 μm , which is calculated by the mass increment after ultrasonic spray-coating. In this section, the critical energy release rate G_c of 58.2 J/m^2 is captured by the peeling test mentioned previously.

Second, for one stent, namely PLLA-coated AZ31-SIN stent, the process of delamination was further investigated. The traction of the cohesive element layer during crimping and expansion were plotted and divided in the local coordinate system. The sequence of damaging and deleting the cohesive element during the process of coating debonding were evaluated.

Third, as different coating material properties and stent materials influence the adhesion interface states and deformations of the coatings, the influence of stent design and material on coating deformation behavior was investigated. For the 3D models, we build up three different stent platforms: AZ31-SIN stent, JDBM-SIN stent,

and JDBM-OPT stent, coated with PLLA with 10 μm thickness. To present the various behavior of coating deformation on a different platform, we assumed another smaller interface fracture energy G_c of 43.5 J/m^2 .

Furthermore, to investigate the influence of coating materials and thickness on coating peeling, we combined two materials (PLLA and PLGA) and three coating thicknesses (5, 10, and 15 μm) with the three stent platforms (AZ31-SIN, JDBM-SIN, and JDBM-OPT) for 18 simulation scenarios. The range of coating thickness is based on the current commercial stent coating thicknesses, and can provide a reference for future coating process optimization. For each scenario, a critical interface fracture energy G_c' , the minimum value of G_c to avoid coating delamination during the expansion step, was calculated and compared to other scenarios.

RESULTS

Simulation Predicting and Experiment Validation.

Three FEA scenarios were simulated and validated by experiments, as shown in Figure 5. The first row is the SIN stent coated with PLLA (a–c), the second row is the same stent coated with PLGA (d–f) and the last row is the OPT stent coated with PLGA (g–i). All three groups of stents were crimped to an outer diameter of 1.3 mm and after that be expanded to an inner diameter of 3.1 mm.

The distributions of the maximum principal stress of the PLLA coating are shown in two different perspectives (Figure 5a, b). The predicted fractures and delamination of PLLA coatings in SIN stent were similar to the experiment (Figure 5c). As shown in Figure 5d, the PLGA coating in the SIN stent should remain integrated after the expansion, which was also

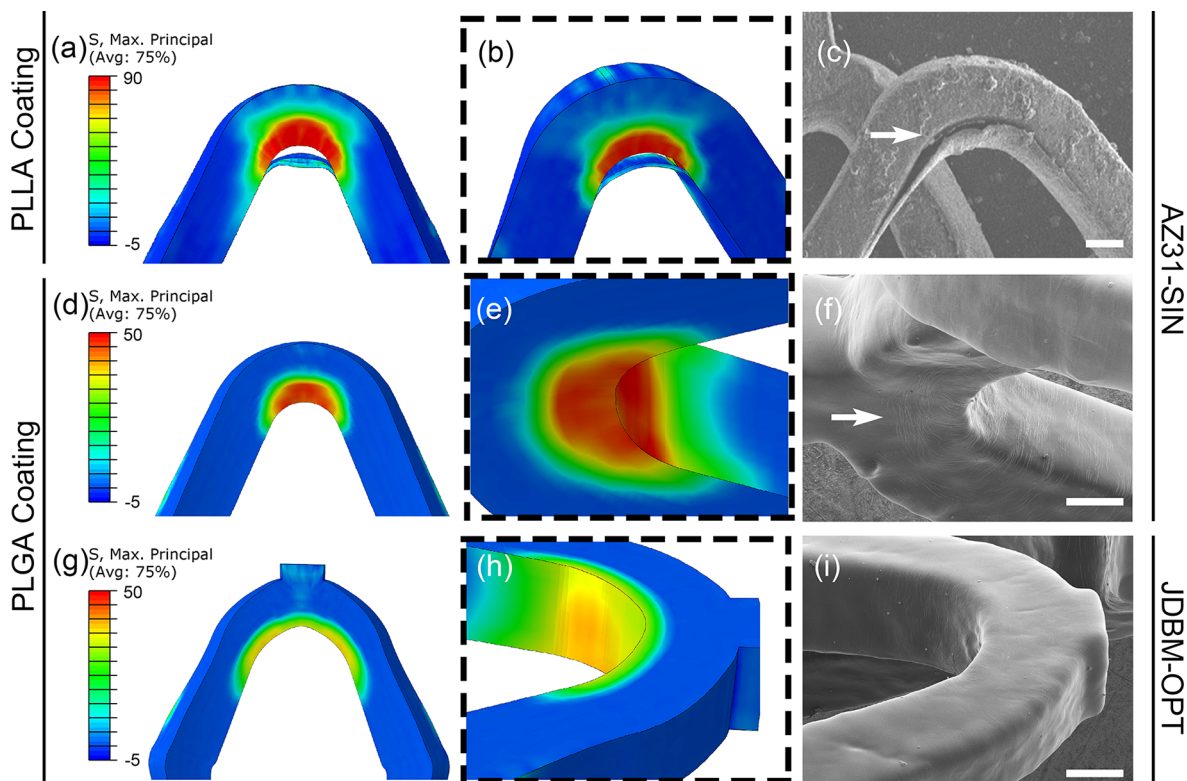


Figure 5. Maximum principal stress distributions on the polymer coatings after expansion and the SEM images for coating delamination (scale bar represents 100 μm). (a, b) The delamination of PLLA coating on the AZ31-SIN stent is consistent with (c) the SEM image, where the arrow indicates the delamination phenomenon. The PLGA coatings maintained their integrity on the (d) JDBM-SIN stent and (g) JDBM-OPT stent, whereas the coating on the SIN stent has higher (e) stresses and (f) microcracks with respect to (h, i) the OPT stent, where the arrow indicates the microcracks.

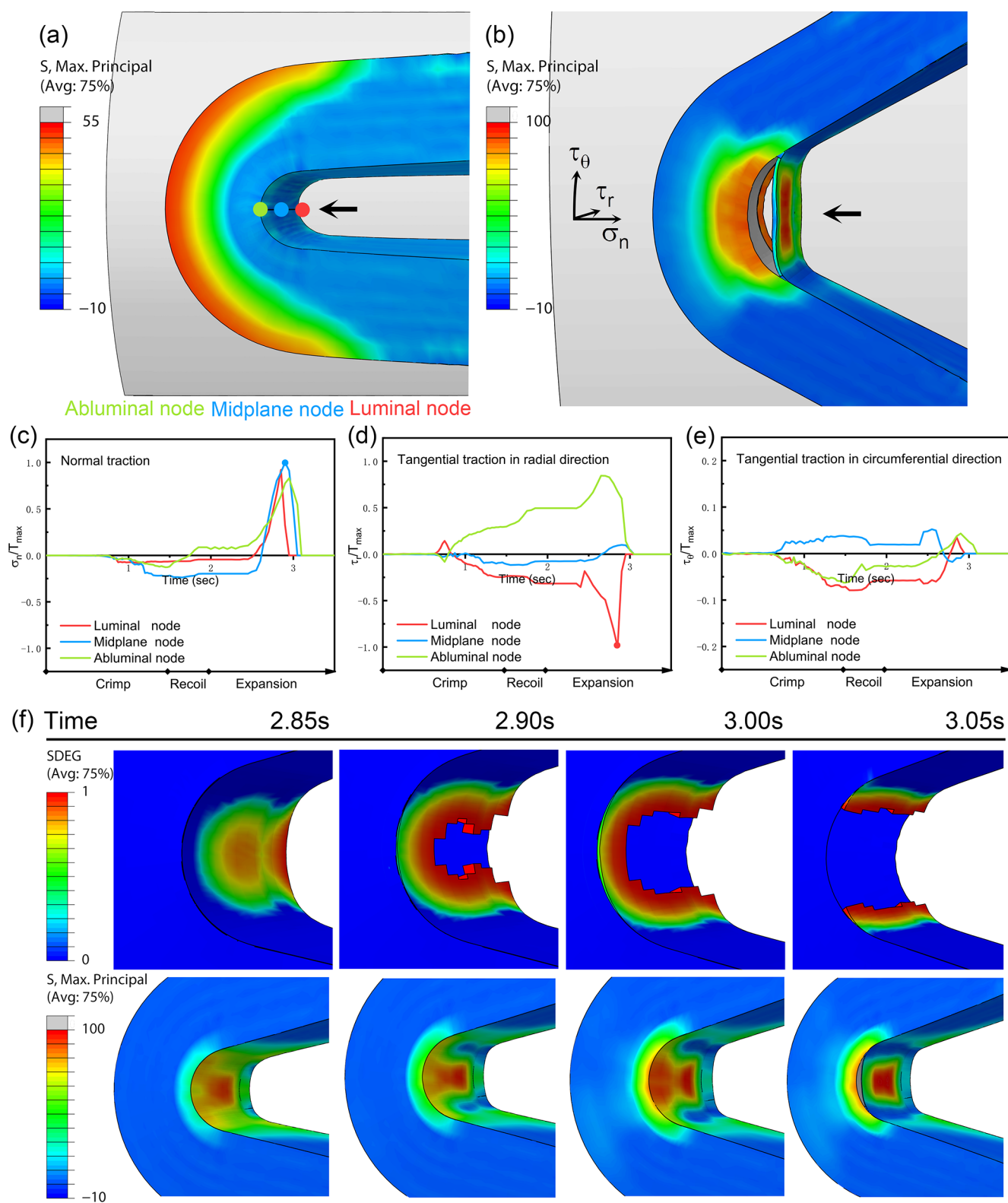


Figure 6. Maximum principal stress distributions of polymer coating after (a) crimping and (b) expansion. Three collinear dots show the locations of representative nodes of the cohesive layer, indicated by the black arrow in a. The coating delamination is indicated by the black arrow in b. (c) Normal traction (σ_n), (d) tangential traction in the radial direction (τ_r), and (e) tangential traction in the circumferential direction (τ_θ) for the three nodes, respectively. (f) Sequence of stiffness degradation distribution (SDEG) of the cohesive elements and maximum principal stress distribution of the coating elements during the initial period of the delamination.

confirmed by SEM observations (Figure 5f). Furthermore, the simulation found coating stress concentration near the inside edge of the stent bow (Figure 5d, e). In the SEM observation,

dense microcracks exhibit a similar pattern to the contour of the stress distribution in the same region (Figure 5f). The density of the microcracks looked consistent with the

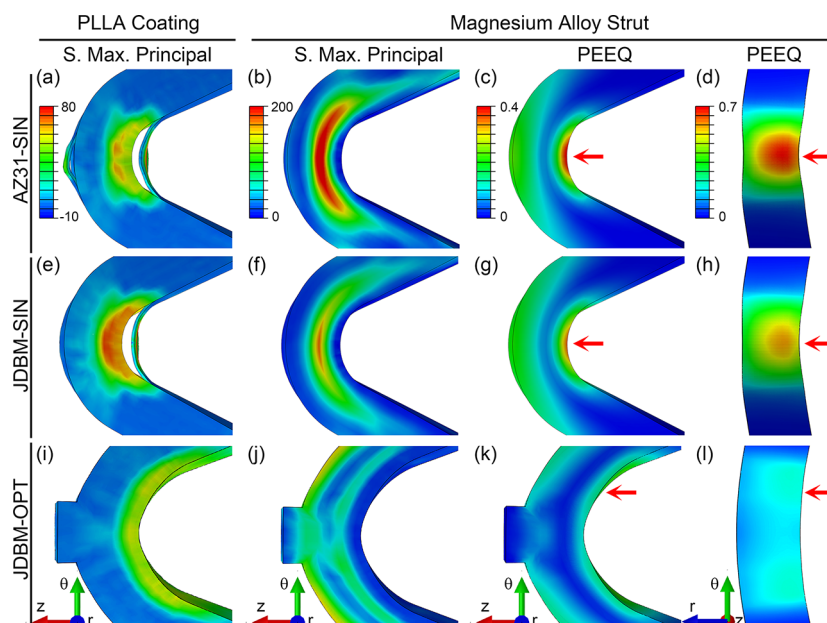


Figure 7. Maximum principal stress distributions of PLLA coatings with a thickness of $10\ \mu\text{m}$ on the (a) AZ31-SIN stent (e), JDBM-SIN stent and (i) JDBM-OPT stent expanded to the inner diameter of 3.1 mm and recoiled, with an interface fracture energy G_c of $43.5\ \text{J}/\text{m}^2$. The max principal stress in the stents is shown in panels b, f, and j. The equivalent plastic strain (PEEQ) distributions of the abluminal strut surface are shown in panels c, g, and k, and for the lateral strut surface in panels d, h, and l. Two legends are used to highlight the difference in abluminal and lateral surface; the locations of maximum PEEQ are marked by three red arrows.

distribution of maximum principal stress on the coating surface.

The comparison between the PLGA coatings in SIN and OPT stent (Figure 5d, e) shows that the coating in the OPT stent has a much lower peak stress than that in the SIN stent (33 MPa vs 49 MPa), and no microcracks can be observed in SEM image (Figure 5i).

Stress Fluctuation during Crimping and Expansion.

The deformation and maximum principal stress distribution of PLLA coating in SIN stent after crimping and expansion are shown in Figure 6. Although the coating remained intact after crimping (Figure 6a), it had delamination inside the strut bow and was fractured at the inside edge of the coating after the expansion (Figure 6b).

Three collinear nodes were selected from the cohesive layer at luminal (red), midplane (blue), and abluminal (green) location to analyze the stress in the cohesive layer. According to the local coordinate system defined in Figure 5b (n , r , and θ in normal, radial, and circumferential direction), the tractions of these nodes in the three directions are shown in Figure 5c–e, respectively. The normal traction σ_n of the three nodes were in compressive state during crimping and recoil. During expansion σ_n of these nodes changed to a tensile state and increased rapidly, and the midplane node reached the T_{max} at 2.80 s, then the corresponding CZE was damaged and deleted in sequence. The peak σ_n of the luminal and the abluminal node reached are $0.96T_{\text{max}}$ and $0.82T_{\text{max}}$, respectively. This result shows that the normal traction is not the only reason for the coating delamination at the luminal and abluminal locations. As for the tangential traction in the radial direction (τ_r), the midplane node reached a peak value of $0.14T_{\text{max}}$ during the expansion (Figure 6d). However, τ_r of the luminal node reached $-T_{\text{max}}$ at 2.85 s, almost at the same time it reached the peak value of σ_n . The corresponding CZEs were then damaged and coating delamination occurred at the

luminal location. The tangential traction τ_r of the abluminal node reached $0.84T_{\text{max}}$ at 2.65 s, earlier than the normal traction got the peak value. In the circumference direction, the tangential tractions (τ_θ) for the three nodes fluctuated around zero because of the geometrical symmetry (Figure 6e).

The sequence of stiffness degradation distribution of cohesive elements and maximum principal stress distribution of the coating elements during the initial period of the delamination revealed the detailed process of cohesive elements degradation (Figure 6f). The midplane node and luminal node got damaged at 2.85 s, but the cohesive layer was still intact. The initial debond of coating appeared in the luminal and middle zone at 2.90 s. Subsequently, the debond of coating spread around and the concentration of stress occurred around the abluminal node at 3.00 s. In the next timeframe, all of the cohesive elements on the symmetric line were deleted and the delamination of coating took place at 3.05 s.

Influence of Stent Design and Material on Coating Deformation.

As for the influence of the stent material and design on the coating deformation, the first column of Figure 7 shows the surface morphology and stress distribution of the PLLA coating after crimping and expansion of the three different stent platforms (AZ31-SIN stent, JDBM-SIN stent, and JDBM-OPT stent). The PLLA coating on the AZ31-SIN stent delaminated at both inside and outside edge of the bow after being deployed (Figure 7a). When the material is changed from AZ31 alloy to JDBM, the coating on JDBM-SIN is delaminated at the inside edge, whereas the outside edge of coating remained intact (Figure 7e). On the other hand, when the stent material is JDBM but the stent design is changed to OPT, all the PLLA coating on JDBM-OPT stent remains intact after balloon expansion and recoil (Figure 7i). The peak value of the maximum principal stress of coatings decreased from 76.2 to 56.73 MPa (Figure 7e, i).

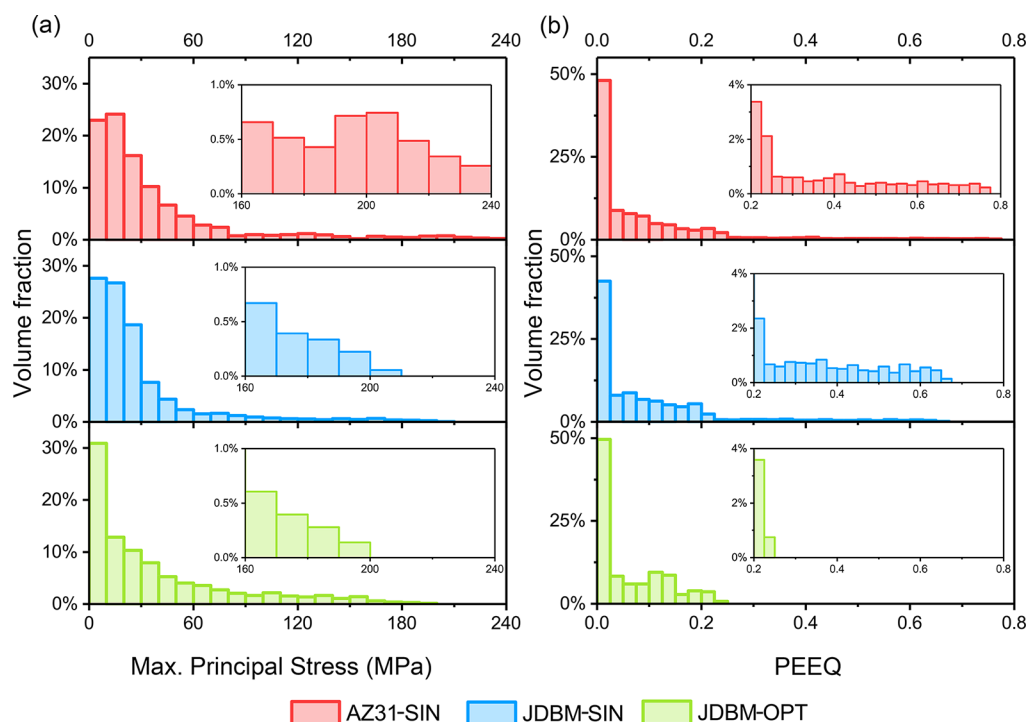


Figure 8. Volume fraction of (a) maximum principal stress, and (b) PEEQ in AZ31-SIN stent (red), JDBM-SIN stent (blue), and JDBM-OPT stent (green).

To further disclose the influence of stent material and design, the struts of AZ31-SIN, JDBM-SIN and JDBM-OPT stent were isolated to compare the distribution of maximum principal stress ($S_{\text{Max. Principal}}$) and equivalent plastic strain (PEEQ) (Figure 7b, c, f, g) in the stent after expansion and recoil. The same design and the same elastic modulus of alloys generated similar patterns of stress and strain for AZ31-SIN and JDBM-SIN stent. The peak values of the max principal stress of AZ31-SIN and JDBM-SIN stent are 245.3 and 203.6 MPa, respectively. And the corresponding peak values of equivalent plastic strain are 0.779 and 0.633, respectively. Meanwhile, the locations of peak stress are located at the center part of the strut corner and the locations of peak plastic strain are located at the symmetric line of lateral surface (Figure 7d, h). When the stent design is considered, the maximum value of the maximum principal stress of JDBM-OPT stent was decreased to 193.4 MPa (Figure 7j), and the PEEQ was significantly reduced to 0.232 (Figure 7k), compared to the JDBM-SIN stent. Meanwhile, the stress concentration was separated into two symmetrical parts and the location of peak value moved away from the center (Figure 7l).

Considering that the value of the single integration point cannot reveal the deformation behavior comprehensively, the statistics of the volume fraction of stent elements stress are shown in Figure 8. The volume percentage of high stress (≥ 160 MPa), of AZ31-SIN stent, JDBM-SIN stent, and JDBM-OPT are 4.14, 1.71, and 1.42%, respectively (Figure 8a) and the percentage of high plastic deformation (≥ 0.2), of them are 14.2, 12.3, and 4.36% respectively (Figure 8b). These statistics disclose that the AZ31-SIN stent exhibits more severe stress concentration behavior than JDBM-SIN stent. The JDBM-OPT stent decreased the concentration of PEEQ significantly and reduced the stress to a certain extent

compared to JDBM-SIN stent. Stent design plays a crucial factor in the deformation behavior of stent and coating.

Influence of Coating Materials and Thickness. The critical interface fracture energy G_c' of each combination of coating materials, thicknesses and stent platforms was evaluated by multiple tentative simulations (Figure 9).

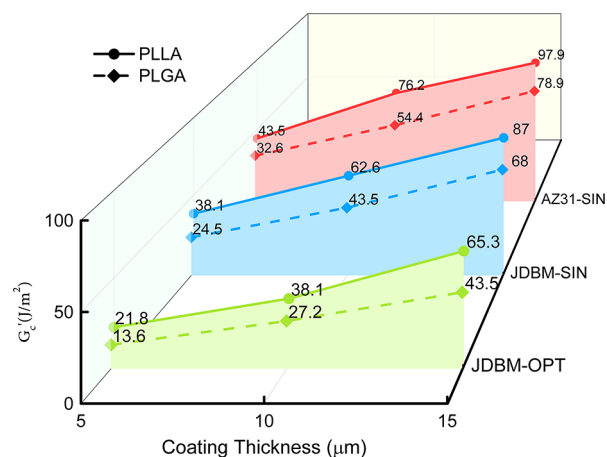


Figure 9. Critical interface fracture energy G_c' required to avoid delamination for the combination of different polymer coatings, coating thickness, and stent types.

Among them, the JDBM-OPT stent coated with PLGA of the thickness of 5 μm required an interface fracture energy G_c' that is not less than 13.6 J/m^2 . Therefore, the coating remains intact during the deformation. With the increase in coating thickness, the critical interface strength increased accordingly and the critical interface strength required for the PLGA coating of a thickness of 10 and 15 μm increased to 27.2 J/m^2 and 43.5 J/m^2 , respectively. Because the PLLA coating has

higher elastic modulus and yield strength than those of the PLGA coating (2.71 MPa vs 1.58 MPa; 67 MPa vs 29 MPa), the critical interface fracture energy of PLLA is higher than that of PLGA, based on the same stent platform. In addition, when the stent material and design are considered, the analysis of the critical interface fracture energy G_c' is consistent with the previous comparison of the stress distribution statistics (Figure 8). Although both the design and the material of the stent affect the critical interface fracture energy, the primary factor is the design and the influence of the stent material is subordinate relatively. For example, the critical interface fracture energies of PLLA with a thickness of 15 μm on these stent platforms are 65.3, 87, and 97.9 J/mm^2 , respectively (Figure 9). The critical interface fracture increased by 33.2% due to the replacement of the stent design while substituting the AZ31 for JDBM, the critical interface fracture only increased by 12.3%.

DISCUSSION

The study of stent coating delamination is important because the delamination damages the coating integrity and then influences the drug delivery adversely.^{19,21,40} Furthermore, the coating delamination of biodegradable magnesium alloy stents can accelerate the localized corrosion of the stent platform. This study applied a 3D finite element model to predict the coating delamination for three scenarios, and the results are well-compatible to experimental tests (Figure 5). Considering that the FEA framework includes a series of parameters, such as the material properties of the stent and coating, the thickness of the coating and the interface fracture energy G_c , the validated simulation proved the robustness, accuracy and compatibility of the proposed CZM framework. As far as the authors know, this is the first work using a 3D model to evaluate the coating delamination of cardiovascular stents.

Compared to the adhesion properties between ChronoFlex AL and 316L stainless steel captured via peeling test by C. Hopkins et al.,³⁰ our interface fracture energy G_c is much higher (58.2 J/m^2 vs 29.6 J/m^2 for dry sample). The primary cause is that the fluoride acid corrodes the sample surface. The roughness of fluoride magnesium is higher than polished stainless steel, which leads to higher interface fracture energy G_c .¹⁴

The 3D model revealed more information about coating delamination which 2D model cannot find, because 3D model includes the stent thickness, and stent-balloon contact and friction. As shown in Figure 6, coating delaminated from the inside edge of strut bow and fractured at the inside edge of coating after expansion. This phenomenon is concurrent with the 2D results.^{29,31,32} The 3D result shows that the normal tractions at luminal and abluminal location are not the only reason for the coating delamination there. The sequence of stiffness degradation distribution of cohesive elements during the initial period of the delamination provided the detailed cohesive elements damaging process (Figure 6f). The contact between coating and balloon plays an important factor on the tangential tractions in the initial phase of delamination. Furthermore, these sequences reveal that the debonding is not instantaneous, but is an incremental process that starts from luminal node toward the abluminal location. This inference is ignored in the 2D analysis. It is worth noting that the radial direction is perpendicular to 2D models, which means that the τ_r will be assumed to be zero in the 2D simulation.

Our analyses showed the influence of the material and the design of the stent platform on coating delamination. Due to the higher yield point of AZ31 compared to JDBM (175 MPa vs 122 MPa), the plastic strain accumulative zone of the AZ31-SIN stent spreads to the adjacent area slower than JDBM stent, resulting in a smaller plastic deformation zone with a higher plastic deformation peak (Figures 7d, h and 8b). Because of the concentrated severe plastic deformation, the strain gradients on the surface of the stent bow become sharp and the interfaces between the coating and the stent have higher shear stress, which will accelerate the damaging of cohesive elements and result in the coating delamination. Furthermore, the local stress concentration of the coating leads to more microcracks in the deformed area, which is a potential problem for the application of the biodegradable magnesium alloy stents. Compared with the distinction between the two magnesium alloys AZ31 and JDBM, the design of stent plays a prominent role in the deformation. The distributions of Max. Principal Stress and PEEQ display completely different patterns between OPT and SIN stents (Figure 7j, k). Because of the design of the salient contour, the external deformation of the OPT stent is spread out to the two shoulders from the center area. The gradient width strut contour scattered the deformation center to the opposite sides (Figure 7k, l). The percentage of high plastic deformation of OPT stent is 4.36% (Figure 8b). The numbers confirm that the high plastic deformation section of the stent decreases sharply when the deformation concentrated area is dispersed to both sides. The plastic deformation in the concentration was evenly distributed to vast areas, resulting in the strain gradient on the stent surface become gentleness, which provides more favorable conditions for the adhesion of the coating.

The influence of polymer coating is also important to control the coating delamination. The analysis of the thickness and type of polymer coating is concurrent with the previous 2D result,^{29,31} i.e., the thicker the coating, the higher the elastic modulus and yield strength of the coating, the more unfavorable the adhesion of the polymer coating on the surface of the stent. More specifically, PLLA is a semicrystalline polymer with high rigidity, whereas PLGA is an amorphous polymer with a soft structure. Mechanical degradation could occur because of the deformation and stress concentration, which will accelerate the asymmetric degradation.^{7,11} PLGA coating with intact adhesion and low stress distribution is more beneficial to uniform protection and degradation for magnesium stent, compared to PLLA coating. Moreover, degradation of magnesium matrix could accelerate the drug release of PLGA coating to overcome the limitation for further clinical application.¹⁶ In brief, the stent design that well-matches coating properties can help improve the clinical outcome of biodegradable Mg alloy stents.

This study has some limitations. First, the zero-thickness cohesive elements are sensitive to mass scaling in 3D modeling. In our work the target time increment is 2×10^{-6} s, a larger target time increment could lead to unstable degradation process of the cohesive elements, which means the computational time of 3D simulation is much higher than in a 2D space. Second, the balloon is simplified to a cylinder surface. The 3-fold balloon will lead to higher friction force on the coating surface, especially in the circumferential direction. Third, it can be observed that the gap located in the inside edge of the corner shown in the FEA result (Figure 5b) is smaller than that in the SEM image (Figure 5c). This comes

from the errors introduced during laser-cutting and coating spray, as well as the asymmetric deformation of crimping and expansion. Fourth, the property of the polymer coating is in dry conditions, considering that the validation experiment is carried out in vitro without liquid. When a stent is implanted, the material property of PLGA and PLLA will change after immersion in blood and the interface strength between coating and stent will be reduced by hydration. Moreover, the critical interface fracture energy G_c' (Figure 9) is an approximation value rather than a precise range, for reducing the amount of calculation.

CONCLUSIONS

This study provides an easily grasped and intelligible framework for understanding the deformation of both coating and stent struts, distinguishing the most important among the multiplying parameters, predicting delamination behavior, and providing guidelines for stent and coating designers.

The significant findings for the polymer coated biodegradable magnesium alloy cardiovascular stents are summarized as follows:

- (1) The debonding process started from luminal location then extended to abluminal node, driven by the contact between balloon and coating.
- (2) JDBM with lower yield strength performed a more uniform strain and is more favorable for adhesion of the coating compared to the commercial magnesium alloy made of AZ31.
- (3) Shape optimization of the stent improves the strain and stress distribution of the coating observably, avoiding coating delamination.
- (4) PLGA coating with lower elastic modulus and yield strength, compared to PLLA polymer, tends to better follow the deformation of the stent and to adhere on the surface tightly.
- (5) A reduction in coating thickness and an increase in stent-coating interface strength improves the resistance to delamination.

AUTHOR INFORMATION

Corresponding Authors

*E-mail: wei.wu2@utsa.edu.

*E-mail: gyyuan@sytu.edu.cn.

ORCID

Chenxin Chen: 0000-0001-8751-0617

Jia Pei: 0000-0002-5256-2895

Hua Huang: 0000-0002-2520-8938

Guangyin Yuan: 0000-0002-2443-8408

Author Contributions

[†]C.C. and J.T. contributed equally to this work.

Notes

The authors declare no competing financial interest.

ACKNOWLEDGMENTS

The authors acknowledge Dr. Pasquale Vena and Dr. Dario Gastaldi for the support in the peeling test. This work was financially supported by the National Key Research and Development Program of China (2016YFC1102103), Science and Technology Commission of Shanghai Municipality (17XD1402100, 17DZ2200200), the National Natural Science

Foundation of China (51501115, 51701041), and Politecnico di Milano International Fellowships Program (PIF).

REFERENCES

- (1) Stefanini, G. G.; Holmes, D. R., Jr. Drug-eluting coronary-artery stents. *N. Engl. J. Med.* **2013**, *368* (3), 254–65.
- (2) Palmerini, T.; Benedetto, U.; Biondi-Zoccai, G.; Della Riva, D.; Bacchi-Reggiani, L.; Smits, P. C.; Vlachojannis, G. J.; Jensen, L. O.; Christiansen, E. H.; Berencsi, K.; Valgimigli, M.; Orlandi, C.; Petrou, M.; Rapezzi, C.; Stone, G. W. Long-Term Safety of Drug-Eluting and Bare-Metal Stents: Evidence From a Comprehensive Network Meta-Analysis. *J. Am. Coll. Cardiol.* **2015**, *65* (23), 2496–507.
- (3) Im, S. H.; Jung, Y.; Kim, S. H. Current status and future direction of biodegradable metallic and polymeric vascular scaffolds for next-generation stents. *Acta Biomater.* **2017**, *60*, 3–22.
- (4) Wykrzykowska, J. J.; Kraak, R. P.; Hofma, S. H.; van der Schaaf, R. J.; Arkenbout, E. K.; Ijsselmuiden, A. J.; Elias, J.; van Dongen, I. M.; Tijssen, R. Y. G.; Koch, K. T.; Baan, J., Jr.; Vis, M. M.; de Winter, R. J.; Piek, J. J.; Tijssen, J. G. P.; Henriques, J. P. S. Bioresorbable Scaffolds versus Metallic Stents in Routine PCI. *N. Engl. J. Med.* **2017**, *376* (24), 2319–2328.
- (5) Ali, Z. A.; Serruys, P. W.; Kimura, T.; Gao, R.; Ellis, S. G.; Kereiakes, D. J.; Onuma, Y.; Simonton, C.; Zhang, Z.; Stone, G. W. 2-year outcomes with the Absorb bioresorbable scaffold for treatment of coronary artery disease: a systematic review and meta-analysis of seven randomised trials with an individual patient data substudy. *Lancet* **2017**, *390* (10096), 760–772.
- (6) Kereiakes, D. J.; Ellis, S. G.; Metzger, C.; Caputo, R. P.; Rizik, D. G.; Teirstein, P. S.; Litt, M. R.; Kini, A.; Kabour, A.; Marx, S. O.; Popma, J. J.; McGreevy, R.; Zhang, Z.; Simonton, C.; Stone, G. W. 3-Year Clinical Outcomes With Everolimus-Eluting Bioresorbable Coronary Scaffolds: The ABSORB III Trial. *J. Am. Coll. Cardiol.* **2017**, *70* (23), 2852–2862.
- (7) Wang, P. J.; Ferralis, N.; Conway, C.; Grossman, J. C.; Edelman, E. R. Strain-induced accelerated asymmetric spatial degradation of polymeric vascular scaffolds. *Proc. Natl. Acad. Sci. U. S. A.* **2018**, *115* (11), 2640–2645.
- (8) Mao, L.; Shen, L.; Niu, J.; Zhang, J.; Ding, W.; Wu, Y.; Fan, R.; Yuan, G. Nanophasic biodegradation enhances the durability and biocompatibility of magnesium alloys for the next-generation vascular stents. *Nanoscale* **2013**, *5* (20), 9517–22.
- (9) Zheng, Y. F.; Gu, X. N.; Witte, F. Biodegradable metals. *Mater. Sci. Eng., R* **2014**, *77* (0), 1–34.
- (10) Esmaily, M.; Svensson, J. E.; Fajardo, S.; Birbilis, N.; Frankel, G. S.; Virtanen, S.; Arrabal, R.; Thomas, S.; Johansson, L. G. Fundamentals and advances in magnesium alloy corrosion. *Prog. Mater. Sci.* **2017**, *89*, 92–193.
- (11) Laycock, B.; Nikolić, M.; Colwell, J. M.; Gauthier, E.; Halley, P.; Bottle, S.; George, G. Lifetime prediction of biodegradable polymers. *Prog. Polym. Sci.* **2017**, *71*, 144–189.
- (12) Haude, M.; Erbel, R.; Erne, P.; Verheye, S.; Degen, H.; Bose, D.; Vermeersch, P.; Wijnbergen, I.; Weissman, N.; Prati, F.; Waksman, R.; Koolen, J. Safety and performance of the drug-eluting absorbable metal scaffold (DREAMS) in patients with de-novo coronary lesions: 12 month results of the prospective, multicentre, first-in-man BIOSOLVE-I trial. *Lancet* **2013**, *381* (9869), 836–44.
- (13) Haude, M.; Ince, H.; Abizaid, A.; Toelg, R.; Lemos, P. A.; von Birgelen, C.; Christiansen, E. H.; Wijns, W.; Neumann, F. J.; Kaiser, C.; Eeckhout, E.; Lim, S. T.; Escaned, J.; Garcia-Garcia, H. M.; Waksman, R. Safety and performance of the second-generation drug-eluting absorbable metal scaffold in patients with de-novo coronary artery lesions (BIOSOLVE-II): 6 month results of a prospective, multicentre, non-randomised, first-in-man trial. *Lancet* **2016**, *387* (10013), 31–9.
- (14) Jiang, W. S.; Tian, Q. M.; Vuong, T.; Shashaty, M.; Gopez, C.; Sanders, T.; Liu, H. N. Comparison Study on Four Biodegradable Polymer Coatings for Controlling Magnesium Degradation and human Endothelial Cell Adhesion and Spreading. *ACS Biomater. Sci. Eng.* **2017**, *3* (6), 936–950.

- (15) Liu, J.; Zheng, B.; Wang, P.; Wang, X.; Zhang, B.; Shi, Q.; Xi, T.; Chen, M.; Guan, S. Enhanced in Vitro and in Vivo Performance of Mg-Zn-Y-Nd Alloy Achieved with APTES Pretreatment for Drug-Eluting Vascular Stent Application. *ACS Appl. Mater. Interfaces* **2016**, *8* (28), 17842–58.
- (16) Shi, Y. J.; Pei, J.; Zhang, L.; Lee, B. K.; Yun, Y.; Zhang, J.; Li, Z. H.; Gu, S.; Park, K.; Yuan, G. Y. Understanding the effect of magnesium degradation on drug release and anti-proliferation on smooth muscle cells for magnesium-based drug eluting stents. *Corros. Sci.* **2017**, *123*, 297–309.
- (17) Shi, Y.; Zhang, L.; Chen, J.; Zhang, J.; Yuan, F.; Shen, L.; Chen, C.; Pei, J.; Li, Z.; Tan, J.; Yuan, G. In vitro and in vivo degradation of rapamycin-eluting Mg-Nd-Zn-Zr alloy stents in porcine coronary arteries. *Mater. Sci. Eng., C* **2017**, *80*, 1–6.
- (18) Ng, J.; Foin, N.; Ang, H. Y.; Fam, J. M.; Sen, S.; Nijjer, S.; Petraco, R.; Di Mario, C.; Davies, J.; Wong, P. Over-expansion capacity and stent design model: An update with contemporary DES platforms. *Int. J. Cardiol.* **2016**, *221*, 171–9.
- (19) Watanabe, T.; Fujita, M.; Awata, M.; Iida, O.; Okamoto, S.; Ishihara, T.; Uematsu, M. Integrity of stent polymer layer after drug-eluting stent implantation: in vivo comparison of sirolimus-, paclitaxel-, zotarolimus- and everolimus-eluting stents. *Cardiovasc. Intervention Ther.* **2014**, *29* (1), 4–10.
- (20) Levy, Y.; Mandler, D.; Weinberger, J.; Domb, A. J. Evaluation of drug-eluting stents' coating durability—clinical and regulatory implications. *J. Biomed. Mater. Res., Part B* **2009**, *91* (1), 441–451.
- (21) Karanasiou, G. S.; Papafaklis, M. I.; Conway, C.; Michalis, L. K.; Tzafiri, R.; Edelman, E. R.; Fotiadis, D. I. Stents: Biomechanics, Biomaterials, and Insights from Computational Modeling. *Ann. Biomed. Eng.* **2017**, *45* (4), 853–872.
- (22) McHugh, P.; Barakat, A.; McGinty, S. Medical Stents: State of the Art and Future Directions. *Ann. Biomed. Eng.* **2016**, *44* (2), 274–5.
- (23) Bressloff, N. W.; Ragkousis, G.; Curzen, N. Design Optimisation of Coronary Artery Stent Systems. *Ann. Biomed. Eng.* **2016**, *44* (2), 357–67.
- (24) Grogan, J. A.; Leen, S. B.; McHugh, P. E. Optimizing the design of a bioabsorbable metal stent using computer simulation methods. *Biomaterials* **2013**, *34* (33), 8049–60.
- (25) Wu, W.; Petrini, L.; Gastaldi, D.; Villa, T.; Vedani, M.; Lesma, E.; Previtali, B.; Migliavacca, F. Finite element shape optimization for biodegradable magnesium alloy stents. *Ann. Biomed. Eng.* **2010**, *38* (9), 2829–40.
- (26) Wu, W.; Chen, S.; Gastaldi, D.; Petrini, L.; Mantovani, D.; Yang, K.; Tan, L.; Migliavacca, F. Experimental data confirm numerical modeling of the degradation process of magnesium alloys stents. *Acta Biomater.* **2013**, *9* (10), 8730–9.
- (27) Gu, Z.; Li, S.; Zhang, F.; Wang, S. Understanding Surface Adhesion in Nature: A Peeling Model. *Adv. Sci. (Weinh)* **2016**, *3* (7), 1500327.
- (28) Diehl, T. On using a penalty-based cohesive-zone finite element approach, Part I: Elastic solution benchmarks. *Int. J. Adhes. Adhes.* **2008**, *28* (4–5), 237–255.
- (29) Hopkins, C. G.; McHugh, P. E.; McGarry, J. P. Computational investigation of the delamination of polymer coatings during stent deployment. *Ann. Biomed. Eng.* **2010**, *38* (7), 2263–73.
- (30) Hopkins, C.; McHugh, P. E.; O'Dowd, N. P.; Rochev, Y.; McGarry, J. P. A combined computational and experimental methodology to determine the adhesion properties of stent polymer coatings. *Comput. Mater. Sci.* **2013**, *80*, 104–112.
- (31) Hopkins, C.; Sweeney, C. A.; O'Connor, C.; McHugh, P. E.; McGarry, J. P. Webbing and Delamination of Drug Eluting Stent Coatings. *Ann. Biomed. Eng.* **2016**, *44* (2), 419–31.
- (32) Wu, W.; Mercuri, M.; Pedroni, C.; Migliavacca, F.; Petrini, L. A Computational Study to Investigate Debonding in Coated Bioresorbable Stents. *J. Mech. Med. Biol.* **2015**, *15* (2), 1540015.
- (33) Zhang, J.; Kong, N.; Shi, Y.; Niu, J.; Mao, L.; Li, H.; Xiong, M.; Yuan, G. Influence of proteins and cells on in vitro corrosion of Mg–Nd–Zn–Zr alloy. *Corros. Sci.* **2014**, *85* (0), 477–481.
- (34) Liu, F.; Chen, C.; Niu, J.; Pei, J.; Zhang, H.; Huang, H.; Yuan, G. The processing of Mg alloy micro-tubes for biodegradable vascular stents. *Mater. Sci. Eng., C* **2015**, *48*, 400–7.
- (35) Zhang, J.; Li, H.; Wang, W.; Huang, H.; Pei, J.; Qu, H.; Yuan, G.; Li, Y. The degradation and transport mechanism of a Mg–Nd–Zn–Zr stent in rabbit common carotid artery: A 20-month study. *Acta Biomater.* **2018**, *69*, 372–384.
- (36) Paryab, N.; Cronin, D.; Lee-Sullivan, P.; Ying, X.; Boey, F. Y. C.; Venkatraman, S. Uniform Expansion of a Polymeric Helical Stent. *J. Med. Devices* **2012**, *6* (2), 021012.
- (37) De Falco, P.; Barbieri, E.; Pugno, N.; Gupta, H. S. Staggered Fibrils and Damageable Interfaces Lead Concurrently and Independently to Hysteretic Energy Absorption and Inhomogeneous Strain Fields in Cyclically Loaded Antler Bone. *ACS Biomater. Sci. Eng.* **2017**, *3* (11), 2779–2787.
- (38) Wei, W.; Petrini, L.; Altomare, L.; Fare, S.; Tremamunno, R.; Yu, Z.; Migliavacca, F. Modeling and Experimental Studies of Peeling of Polymer Coating for Biodegradable Magnesium Alloy Stents. *Rare Met. Mater. Eng.* **2014**, *43* (12), 2877–2882.
- (39) Lucchini, R.; Cattarinuzzi, E.; Maraghechi, S.; Gastaldi, D.; Adami, A.; Lorenzelli, L.; Vena, P. Delamination phenomena in aluminum/polyimide deformable interconnects: In-situ micro-tensile testing. *Mater. Des.* **2016**, *89*, 121–128.
- (40) Gu, X.; Mao, Z.; Ye, S. H.; Koo, Y.; Yun, Y.; Tiasha, T. R.; Shanov, V.; Wagner, W. R. Biodegradable, elastomeric coatings with controlled anti-proliferative agent release for magnesium-based cardiovascular stents. *Colloids Surf., B* **2016**, *144*, 170–179.